Nuclear Instruments and Methods in Physics Research A 595 (2008) 359–374

Contents lists available at ScienceDirect

Nuclear Instruments and Methods in Physics Research A

journal homepage: www.elsevier.com/locate/nima

Separation of crystal signals into scintillation and Cherenkov components

N. Akchurin [a], A. Astwood [a], A. Cardini [b], G. Ciapetti [c], R. Ferrari [d], S. Franchino [d], M. Fraternali [d], G. Gaudio [d], J. Hauptman [e], F. Lacava [c], L. La Rotonda [f], M. Livan [d], E. Meoni [f], H. Paar [g], D. Pinci [c], A. Policicchio [f], S. Popescu [a], G. Susinno [f], Y. Roh [a], W. Vandelli [h], T. Venturelli [f], C. Voena [c], I. Volobouev [a], R. Wigmans [a,*]

[a] Texas Tech University, Lubbock, TX, USA
[b] Dipartimento di Fisica, Università di Cagliari and INFN Sezione di Cagliari, Italy
[c] Dipartimento di Fisica, Università di Roma "La Sapienza" and INFN Sezione di Roma, Italy
[d] Dipartimento di Fisica Nucleare e Teorica, Università di Pavia and INFN Sezione di Pavia, Italy
[e] Iowa State University, Ames, IA, USA
[f] Dipartimento di Fisica, Università della Calabria and INFN Cosenza, Italy
[g] University of California at San Diego, La Jolla, CA, USA
[h] CERN, Genève, Switzerland

ARTICLE INFO

Article history:
Received 6 May 2008
Received in revised form
29 June 2008
Accepted 16 July 2008
Available online 31 July 2008

Keywords:
Scintillating crystals
Cherenkov light
Electromagnetic showers

ABSTRACT

The signals from high-Z scintillating crystals such as $PbWO_4$ and BGO contain a significant Cherenkov component. We investigate methods to determine the contribution of Cherenkov light to the signals generated by high-energy electrons and pions (mips), both statistically and event-by-event. These methods are based on differences in the spectra, the time structure and/or the directionality of the two types of light. The electron signals, and their composition, are also analyzed as a function of the age (or depth) of the shower.

1. Introduction

In a recent paper [1], we demonstrated that a significant fraction of the signals from scintillating lead tungstate ($PbWO_4$) crystals is due to Cherenkov radiation. This was concluded from measurements of the time structure of the signals and the non-isotropic nature of the light generated by high-energy electrons and muons traversing a $PbWO_4$ crystal. The measurements showed that Cherenkov light contributed in that case up to 15% to the signals generated by these particles in the crystal used for these studies, at room temperature. However, for individual events it was not possible to establish this fraction very accurately, mainly as a result of the relatively small numbers of photoelectrons generated in the setup that was used. The reason why we are interested in precise event-by-event measurements of the Cherenkov/scintillation signal ratio is that this ratio is the crucial ingredient for applying these crystals as dual-readout calorimeters [2].

One obvious way to increase the light yield is to increase the amount of deposited energy, for example by absorbing electron showers rather than using the crystal as a $2.5X_0$ thick target, in which the electrons mimic a collection of coherent minimum ionizing particles. However, in another paper we have shown that the anisotropy of the produced light, which formed our most important signature for the Cherenkov component, was greatly reduced in that case [3].

We have repeated the measurements described above with much improved time resolution, in order to study the possibilities for improving the measurement precision of the Cherenkov component on the basis of the time structure of the signals alone. We have also performed tests with another type of crystal ($Bi_4Ge_3O_{12}$, or BGO). The Cherenkov component in the signals from this crystal is much smaller than for $PbWO_4$, but it offers better opportunities to measure its contribution with high precision, because of the large decay time of the scintillation component, and the spectral differences between the two components. These measurements are the topic of the present paper. In Section 2, the detectors and the experimental setup in which they were tested are described, as well as the calibration and data analysis methods that were used. Experimental results

* Corresponding author. Fax: +1 806 742 1182.
E-mail address: wigmans@ttu.edu (R. Wigmans).

0168-9002/$ - see front matter © 2008 Elsevier B.V. All rights reserved.
doi:10.1016/j.nima.2008.07.136

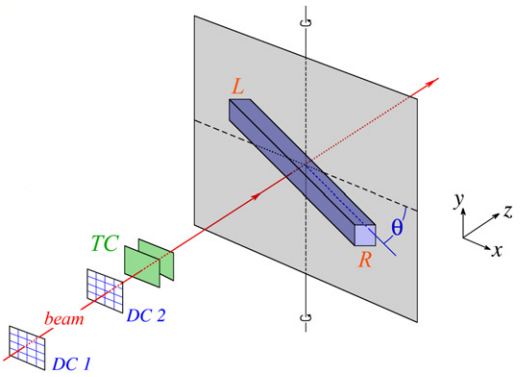

Fig. 1. Experimental setup in which the beam tests of the crystals were performed. The angle θ is negative when the crystal is oriented as drawn here.

are presented in Section 3 for $PbWO_4$ and in Section 4 for BGO. In Section 5, we discuss some instrumental effects common to both crystals. Conclusions are presented in Section 6.

2. Equipment and measurements

2.1. Detectors and beam line

The measurements described in this paper were performed in the H4 beam line of the Super Proton Synchrotron at CERN. Our detector was a high-density crystal. Two different crystals were studied in these tests:

(1) A $PbWO_4$ crystal, produced by the North Crystals company in Apatity (Russia), with a length of 18 cm and a cross-section of $2.2 \times 2.2\,cm^2$. The transverse dimension, relevant for our measurements, corresponded to 2.5 radiation lengths (X_0). The light produced by particles traversing this crystal was read out by two photomultiplier tubes,[1] located at opposite ends. In order to reduce the light trapping effects of the large refractive index of $PbWO_4$ ($n = 2.2$), the PMTs were coupled to the crystal by means of silicone "cookies" ($n = 1.403$).
(2) A $Bi_4Ge_3O_{12}$ (BGO) crystal with a length of 24 cm. This crystal was semi-conical, with one end having a cross-section of $2.4 \times 2.4\,cm^2$, and the other end $3.2 \times 3.2\,cm^2$. The transverse dimension varied between 2.2 and $2.9X_0$, depending on the impact point of the particles. The light generated in this crystal was filtered before being read out. Two different types of filters were used for this purpose, which we will call "Y" (for yellow) and "UV" (for ultraviolet) because of their light transmitting characteristics. The properties of these filters are described in detail in Section 4. For most of the measurements, the UV filter was mounted on the large end face of the crystal (the R side in Fig. 1), and the yellow filter on the small one (the L side). Both sides of the crystal were read out with identical PMTs.[2]

The crystal under study was mounted on a platform that could rotate around a vertical axis. The crystal was oriented in the horizontal plane and the rotation axis went through its geometrical center. The particle beam was also steered through this center, as illustrated in Fig. 1. The angle θ, which is frequently used in the following, represents the angle between the crystal axis and a plane perpendicular to the beam line. The angle increases when the crystal is rotated such that the crystal axis L–R approaches the direction of the traveling beam particles. The crystal orientation shown in Fig. 1 corresponds to $\theta = -30^\circ$.

Two small scintillation counters (TC) provided the signals that were used to trigger the data acquisition system. These trigger counters were 2.5 mm thick, and the area of overlap was $6 \times 6\,cm^2$. A coincidence between the logic signals from these counters provided the trigger. The trajectories of individual beam particles could be reconstructed with the information provided by two small drift chambers (DC1, DC2) which were installed upstream of the trigger counters. This system made it possible to determine the location of the impact point of the beam particles at the calorimeter with a precision of typically ~0.2 mm. About 10 m downstream of the crystal, placed behind about 20 interaction lengths of material, a $50 \times 50\,cm^2$ scintillator paddle served as a muon counter.

2.2. Data acquisition

Measurement of the time structure of the calorimeter signals formed a very important part of the tests described here. In order to limit distortion of this structure as much as possible, we used special 15 mm thick low-loss cables to transport the crystal signals to the counting room. Such cables were also used for the signals from the trigger counters, and these were routed such as to minimize delays in the DAQ system.[3] Other signals, e.g. from the muon counter, were transported through RG-58 cables with (for timing purposes) appropriate lengths to the counting room. The crystal signals were sent into a unity-gain Linear Fan-out unit, output signals of which were used to measure the time structure and the total charge.

The data acquisition system used VME electronics. A single VME crate hosted all the needed readout and control boards. The charge measurements of the crystal signals were performed with a CAEN V792AC QADC module,[4] which offered 12-bit digitization at a sensitivity of 100 fC/count and a conversion time below 10 μs. The signals from the muon counters were integrated and digitized with a sensitivity of 100 fC/count, on a 12-bit LeCroy 1182 module.[5] The timing information of the tracking chambers was recorded with 1 ns resolution in a 16-bit 16-channel LeCroy 1176 TDC.[6]

The time structure of the calorimeter signals was recorded by means of a Tektronix TDS 7254B digital oscilloscope,[7] which provided a sampling capability of 5 GSample/s, at an analog bandwidth of 2.5 GHz, over four input channels. During most of the data taking period only two channels were sampled, at a rate of 2.5 GS/s over a time interval of ~100 ns. For other runs, the oscilloscope gain (scale) was tuned such as to optimize the exploitation of the 8-bit dynamic range, i.e. by choosing the sensitivity such that the overflow rate was ~1%.

The $PbWO_4$ signals were measured over a time interval of 112 ns, during which time 282 data points were collected. The quality of the information obtained in this way is illustrated in Fig. 2, which shows the average time structure of the signals from 50 GeV electron showers.

The BGO signals, which had a considerably longer decay time, were followed over a longer time interval: 560 ns (with a

[1] Hamamatsu R5900U, 10-stage, bialkali photocathode, borosilicate window.
[2] Hamamatsu R1355, square (28 mm), 10-stage, with a $25 \times 25\,mm^2$ bialkali photocathode.
[3] We measured the signal speed to be $0.78c$ in these cables.
[4] http://www.caen.it/nuclear/Printable/data_sheet.php?mod=V792&fam=vme&fun=qdc
[5] http://lecroy.com/lrs/dsheets/1182.htm
[6] http://www.lecroy.com/lrs/dsheets/1176.htm
[7] http://www.tek.com/site/ps/0,,55-13766-SPECS_EN,00.html

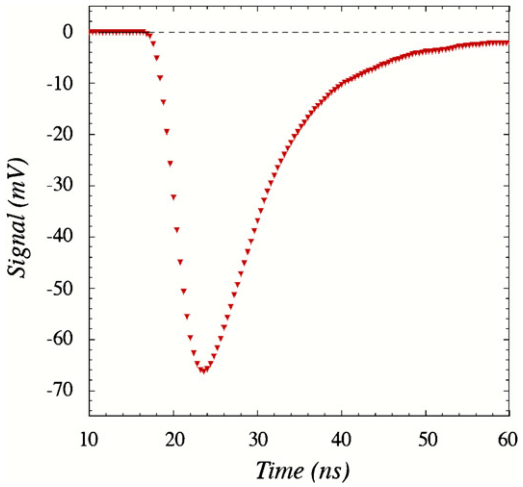

Fig. 2. Average time structure of the signals from 50 GeV electron showers in the lead tungstate crystals.

measurement every 2 ns), or 224 ns (0.8 ns sampling). The trigger logic was implemented through NIM modules and the signals were sent to a VME I/O register, which was also catching the spill and the global busy information. The VME crate was linked to a data acquisition computer through an SBS 620 optical VME-PCI interface.[8] This computer was equipped with a Pentium-4 2 GHz CPU, 1 GB of RAM, and running a CERN SLC 4.3 operating system.[9]

The data acquisition was built around a single-event polling mechanism and performed by a readout program that was streaming physics and on-spill pedestal events into two independent first-in-first-out buffers, built on top of 32 MB shared memories. Our readout scheme optimized the CPU utilization and increased the data taking efficiency thanks to the bunch structure of the SPS cycle, where beam particles were provided to our experiment during a spill of 4.8 s, with a repetition period of 16.8 s.

Owing to the large volume of data produced by the oscilloscope and the poor on-line performance of this instrument, we decided to use it on a multi-event basis. Through the GPIB interface, the digital scope was prepared to acquire events before the extraction and delivery of protons on target. On spill, all events were sequentially recorded in the internal memory of the scope. At the end of the spill, the oscilloscope memory was dumped onto a temporary file, in a network-mounted shared disk. At this point, the file was read out and the data copied in properly formatted areas in the shared-memory buffers, where the information from all the VME modules had already been stored, in real time, by the readout program. In sequence, the recorder programs were then dumping the events to disk and a monitoring program was running in spy mode, on top of the physics shared memory, producing on-line histograms.

With this scheme, we were able to reach, in spill, a data acquisition rate of ~2 kHz, limited by the size of the internal scope buffer. No zero suppression was implemented, so that the event size was constant: ~1.5 MB, largely dominated by the oscilloscope data.

2.3. Experimental data and analysis methods

The purpose of these tests was to split the crystal signals into their scintillation and Cherenkov components. We exploited the following differences between these components to achieve this:

(1) Differences in *directionality*: Contrary to scintillation light, which is emitted isotropically, Cherenkov light is emitted at a characteristic angle by the relativistic (shower) particles that traverse the detector. We measured the signals for different orientations (i.e. angles θ) of the crystal with respect to the particle beam.
(2) Differences in *time structure*: Cherenkov light is prompt, while the scintillation mechanism is characterized by one or several time constants, which determine the pulse shape. Detailed measurements of the time structure were performed (at different angles θ) to study the properties of the prompt component in the signals from the crystals.
(3) Differences in the *spectral properties*: Cherenkov light exhibits a λ^{-2} spectrum, while the scintillation spectrum is characteristic for the crystal in question. Of course, the extent to which these differences may be observed in the measured signals depends also on the wavelength dependence of the quantum efficiency of the light detector. We successfully enhanced the relative contribution of Cherenkov light to the BGO signals with optical filters.

The measurements were performed with 50 GeV e^- and 200 GeV π^+ beams. The angle θ between the crystal axis and the plane perpendicular to the beam line was varied between -80° and 80°, usually in steps of 5°. At each angle, 100 000 events were collected. In addition, 10 000 randomly triggered events provided pedestal information. For each event, the full time structure of the signals from the two PMTs reading the two sides of the crystal was recorded. In addition, ADC information from these channels was measured, as well as the ADC and TDC data from the auxiliary detectors (wire chambers, trigger counters, muon counters).

Off-line, the beam chamber information could be used to select events that entered the crystal in a small (typically $10 \times 10\,mm^2$) region located around its geometric center. The electron beam contained a very small fraction (<1%) of muons, which were eliminated with help of the downstream muon counter. Typically, more than half of the events survived these cuts.

An example of the time structure of the signals measured for electrons in $PbWO_4$ is given in Fig. 2. Fig. 3 shows typical ADC signal distributions for the two types of particles used in these studies, measured by one of the two crystal PMTs. In the electron beam, a ~1% beam contamination of pions produced a mip signal in the crystal (highlighted in Fig. 3a), which was well separated from the signals produced by the showering electrons. For the analysis of these ADC data, we used the *average* signal produced by the electrons. We checked that the choice of other variables used to characterize the signal distribution (e.g. the most probable signal value, or the peak value resulting from a fit) did not change the results significantly.

In order to determine the possible effects of instrumental factors on our results, we also performed a number of dedicated measurements. For example, in order to study the effects of light attenuation in the crystals, detailed scans (in steps of 1 cm) along the full length of the crystals were performed. And to assess the asymmetric effects of the conical shape of the BGO crystal, all measurements were repeated while the two filters were reversed, i.e. the Y filter was mounted on the large ($3.2 \times 3.2\,cm^2$) crystal exit surface, and the UV filter on the small ($2.4 \times 2.4\,cm^2$) exit surface.

In the case of the BGO crystal, we also performed a series of measurements using a much shorter ADC gate than usual, thus reducing the contribution of scintillation light to the (UV) signals.

2.4. Calibration of the detectors

The PMTs used in these measurements were calibrated with 50 GeV electron beams. The calibrations were carried out at $\theta = 0$,

[8] http://www.gefanucembedded.com/products/457
[9] http://linux.web.cern.ch/linux/scientific4/

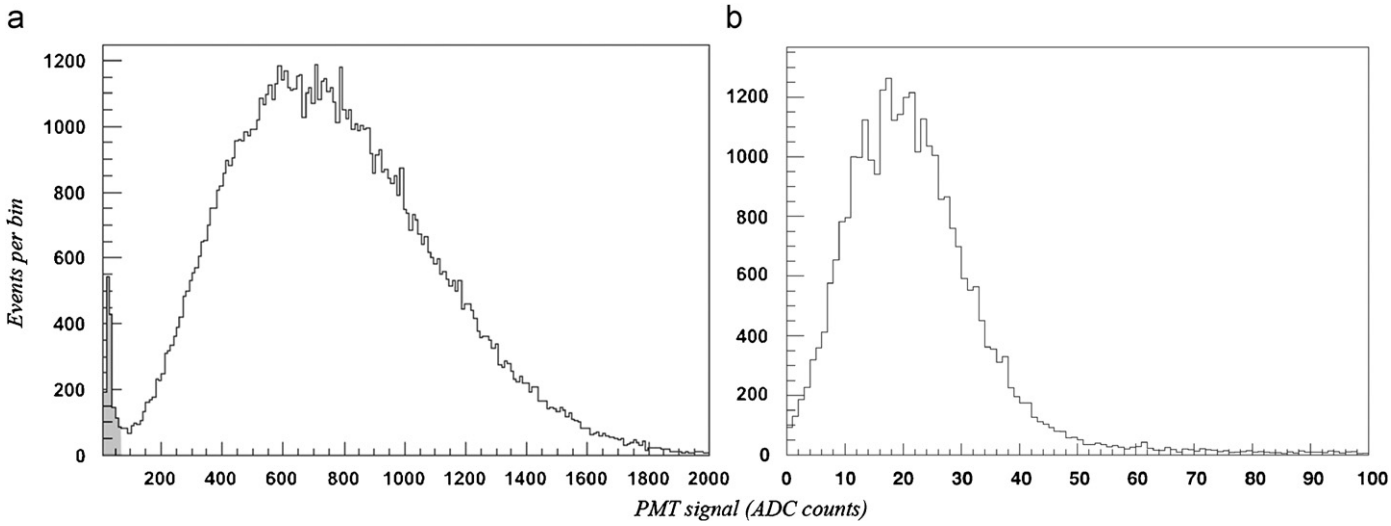

Fig. 3. ADC signal distribution for 50 GeV electrons showering in a $2.5X_0$ thick $PbWO_4$ crystal (a) and for 200 GeV π^+ traversing the BGO crystal (b), measured by one of the PMTs.

i.e. with the crystal oriented perpendicular to the beam line and the beam hitting the center of the crystal. In this geometry, 50 GeV electrons deposited, on average, ~480 MeV in the $PbWO_4$ crystal and 370 MeV in the BGO one.[10] The absolute calibration of the signals generated by the crystal was not a major concern in these tests. On the other hand, in the case of the $PbWO_4$ crystal, it was very important that the gains of the two PMTs, *L* and *R*, which collected the light generated in the crystals at the two opposite ends of the crystal, were equalized. The crystal was oriented such that the beam entered the detector perpendicular to the crystal axis ($\theta = 0$), so that any Cherenkov light generated by the beam particles would be observed in the same proportion by both PMTs. In the case of the BGO crystal, asymmetries between the two crystal exit surfaces (size, filters) eliminated the need for this type of gain equalization. The high voltages were chosen such that the average signals were about 300 ADC counts above the pedestal value. Off-line, the calibration constants of the ADCs (GeV/count) were fine-tuned such as to equalize the responses of the two PMTs, if needed.

For the time structure measurements, no separate calibration effort was performed. We only made sure that the vertical oscilloscope scale was chosen such that no pulse clipping occurred. As the crystals were rotated to larger angles θ, the signals increased and the scale had to be adjusted, e.g. from 100 to 200 to 500 mV full range.

3. Experimental results for $PbWO_4$

3.1. The Cherenkov component in the $PbWO_4$ signals

The time structure of the signals from the $PbWO_4$ crystal depended on the angle of incidence of the particles. Since Cherenkov light was emitted at an angle $\theta_C = 63^\circ$ by the charged, relativistic (shower) particles, the acceptance of this light, and its contribution to the PMT signals from this crystal strongly depended on the angle of incidence of the incoming 50 GeV beam electrons. For the signals from PMT *R*, this contribution was the largest for $\theta \sim 27^\circ$, for PMT *L*, it was the largest for $\theta \sim -27^\circ$ (see Fig. 1).

[10] This was determined with GEANT-4 Monte Carlo calculations.

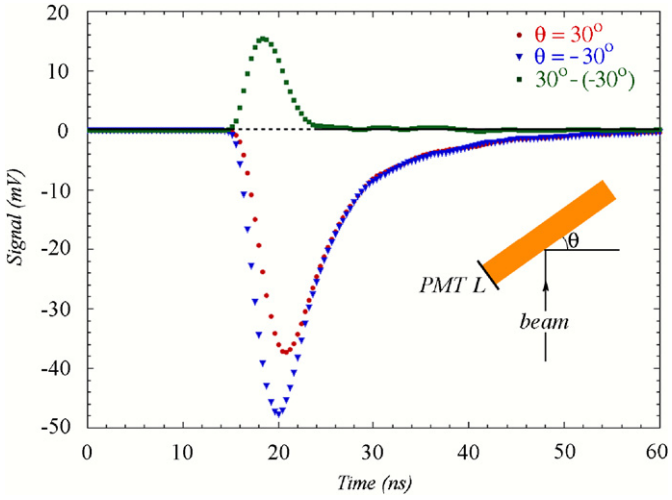

Fig. 4. Time structures of the PMT *L* signals from 50 GeV electrons traversing the $PbWO_4$ crystal at angles $\theta = 30^\circ$ and -30°, respectively, and the difference between these two time distributions.

Fig. 4 shows the average time structure of the signals from 50 GeV electrons in PMT *L*, for angles $\theta = 30^\circ$ and -30°, respectively. The trailing edges of these two signals are in great detail identical. However, the leading edge of the signal recorded at $\theta = -30^\circ$ is considerably steeper, and its amplitude larger than for the signal recorded with the same PMT at $\theta = 30^\circ$.[11] The figure also shows the result of subtracting the signal observed at $\theta = -30^\circ$ from that at $\theta = 30^\circ$. The resulting pulse represents the (inverted) calorimeter response function to the (prompt) Cherenkov component generated by the showering electrons in the $PbWO_4$ crystal. It has a full width at half maximum of 4.7 ns ($\sigma = 2.0$ ns).

The data shown in Fig. 4 were obtained from measurements at a temperature of 45 °C. At that temperature, the scintillation light yield was considerably lower than at room temperature,[12] while

[11] For PMT *R*, the opposite effect was observed: the signals from this PMT had a larger amplitude and a steeper leading edge for $\theta = 30^\circ$ than for $\theta = -30^\circ$.

[12] We measured the scintillation light yield to change by −2.97% per °C [4].

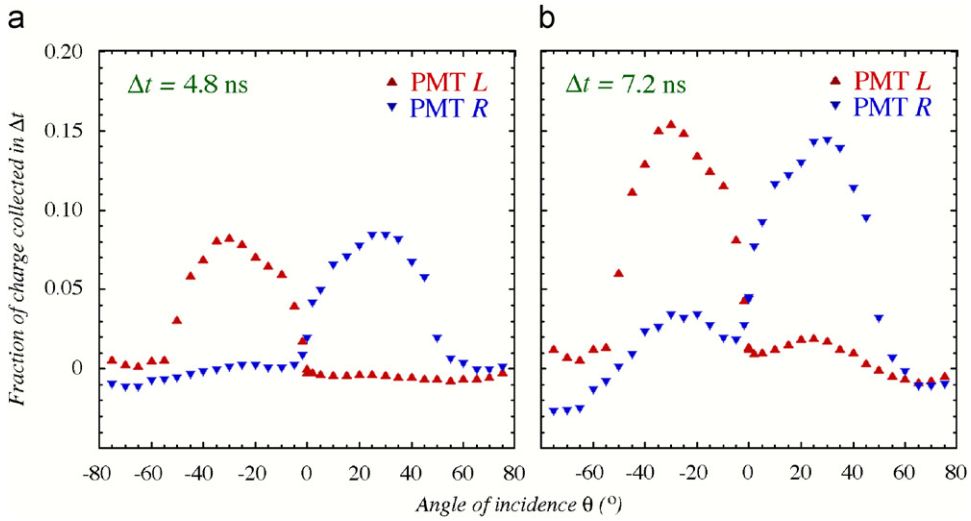

Fig. 5. Fraction of the total charge contained in the PMT signals from 200 GeV pions collected during a time interval Δt after the start of the pulse, as a function of the angle of incidence. Results are given separately for both PMTs, for $\Delta t = 4.8$ ns (a) and 7.2 ns (b). Because of small differences in the PMT characteristics, and because of the arbitrariness of the choice of the starting point of the pulses, the fractions are given modulo an offset, which is slightly different for the two PMTs, and different for the two Δt intervals.

the Cherenkov light yield was temperature independent. The differences between the time structures at $\theta = 30^\circ$ and -30° were thus more pronounced at this high temperature, and this was the reason why we chose these data for this illustrative figure. The measurements on which results are reported in the following were all carried out at room temperature (~21 °C).

3.2. Event-by-event measurements of the Cherenkov fraction

There are several ways in which one may exploit this difference in time structure for determining the relative contribution of Cherenkov light to the signals:

- By measuring the time at which the pulse exceeds a preset threshold value, e.g. 10%, of the amplitude.
- By measuring the steepness of the leading edge, expressed in an appropriate parameterized form.
- By measuring the fraction of the total charge collected in a given time interval, e.g. the first 5 ns.

Some results of the first two methods, obtained with a time resolution that was 6 times worse than available in the present tests, were reported in Ref. [1]. Some results of the third method are given below.

The discriminatory merits of this method are illustrated in Fig. 5, which shows the fraction, $f(\Delta t)$, of the total charge contained in the PMT signals from 200 GeV pions that was collected in a short time interval right after the start of the pulse, as a function of the angle of incidence of the particles. Results are given for two intervals (4.8 and 7.2 ns), separately for both PMTs. Similar results were obtained for a beam of 50 GeV electrons (see Fig. 22). The fraction $f(\Delta t)$ clearly peaks around the angle at which Cherenkov light produced by the particles is most likely to be detected by the PMT in question, i.e. near $\theta = -30^\circ$ for PMT L and at 30° for PMT R. Interestingly, the fraction seems to reach a second local maximum at the "anti-Cherenkov angle" ($\theta = 30^\circ$ for PMT L, -30° for PMT R), at least for the longer gate width. As discussed in Section 5.2, this phenomenon is most likely caused by internal reflections in the crystal.

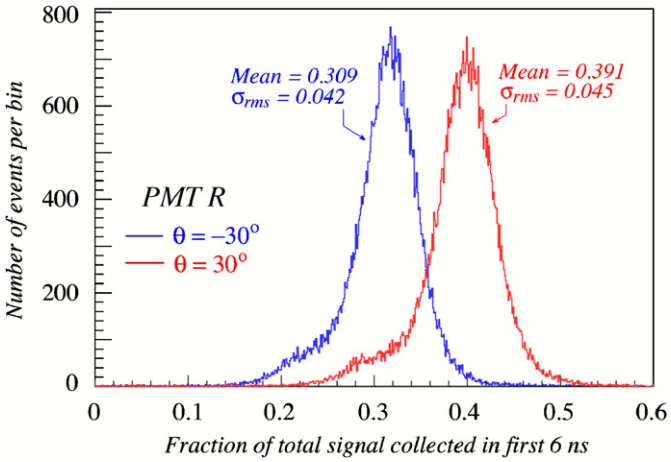

Fig. 6. Distribution of the fraction of the total signal collected during the first 6 ns, f(6 ns), in PMT R, for events in which the 50 GeV electrons deposited 1 GeV in the $PbWO_4$ crystal, for two different orientations of the crystal: $\theta = \pm 30^\circ$.

In order to study the precision with which the Cherenkov fraction could be measured in individual events, we needed a reference signal that consisted (almost) exclusively of scintillation light. We used the signals measured at the anti-Cherenkov angle for this purpose. To eliminate energy dependent effects, we selected electron events that deposited (approximately) the same energy in the crystal, as determined by the reference signal. A comparison of the fluctuations in $f(\Delta t)$ in the signals containing Cherenkov light with those in the reference signals then made it possible to determine the sought precision. As an example, Fig. 6 shows distributions of $f(\Delta t)$ in PMT R, for electrons that deposited 1 GeV in the $PbWO_4$ crystal. The time interval Δt was chosen to be 6 ns. The two distributions concern $\theta = -30^\circ$, at which angle PMT R provided the reference signal, and $\theta = 30^\circ$, the angle at which the Cherenkov content reached its maximum value. In order to quantify the difference, and thus the precision with which the Cherenkov fraction can be measured in individual events, we introduce the *separation power* Π, defined as the ratio of the difference between the two mean values and the average width

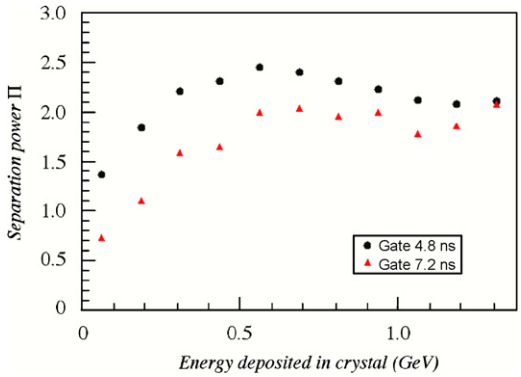

Fig. 7. Precision with which the Cherenkov content of individual events can be measured on the basis of the $f(\Delta t)$ characteristics, as a function of the energy deposited by 50 GeV electrons in the $PbWO_4$ crystal.

(σ_{rms}) of the two distributions. For example, the separation power of the variable f(6 ns) shown in Fig. 6 for 50 GeV electrons is 1.9. Since the average contribution of Cherenkov light to the signals from this crystal at room temperature was ~15% [4], this result translates into a measurement precision of ±8% for individual events.

The same analysis was repeated for different energy deposits by the electrons. Fig. 7 shows that the precision of the event-by-event measurement of the Cherenkov fraction achieved with this method improves somewhat as a function of the deposited energy, but not spectacularly so. This may be due to the fact that as the deposited energy increases, the anisotropy (defined in Eq. (1)), and thus the differences between signals that do and do not contain Cherenkov contributions, tends to decrease. We elaborate on that effect in Section 3.3. The fact that photoelectron statistics is not the main limiting factor for the measurement precision achievable with this method is also illustrated by the fact that for mips (200 GeV pions), we found $\Pi = 2.1$, i.e. a result comparable to that of electrons depositing 30 times more energy in the crystal.

As one might guess from Fig. 4, the rise time of the signals provided another way to exploit differences in the time structure for the purpose of measuring the Cherenkov content. Fig. 8 shows the average time that passed when the amplitude of the PMT signals increased from 10% to 90% of its maximum value, as a function of the angle of incidence of the (50 GeV e^-) beam particles. Results are given separately for the two PMTs. By using inverted angular scales, the angular dependences look identical. The separation power derived from this variable is somewhat smaller than for $f(\Delta t)$. Both for mips and for 50 GeV electrons we found Π~1.3.

The precision with which the Cherenkov fraction can be determined depends not only on the magnitude of the signal, i.e. on the deposited energy, but also on the amount of information used as input for the measurement. For example, the separation power was smaller when only the rise time of the signals was used, compared to the charge fraction $f(\Delta t)$. The latter quantity involved not only the characteristics of the leading edge, but the entire signal. Fig. 9 illustrates that more information led to a larger value of Π. In this case, also the directionality of the light production was included. The figure shows the time difference between the moments at which the signals from the two PMTs crossed a given threshold level, as a function of the orientation of the crystal, i.e. the angle θ. This difference, which as expected changes sign with the angle, increased with the threshold level. It was also typically larger for mips (Fig. 9a) than for electron showers (Fig. 9b). However, the separation power Π is considerably larger than for the previously discussed methods, especially for the electron showers, where $\Pi = 3.3$ for a threshold level of 100 mV (Fig. 9d).

In Fig. 10, the separation power is plotted as a function of the energy deposited in the crystal by 50 GeV electrons. A threshold of

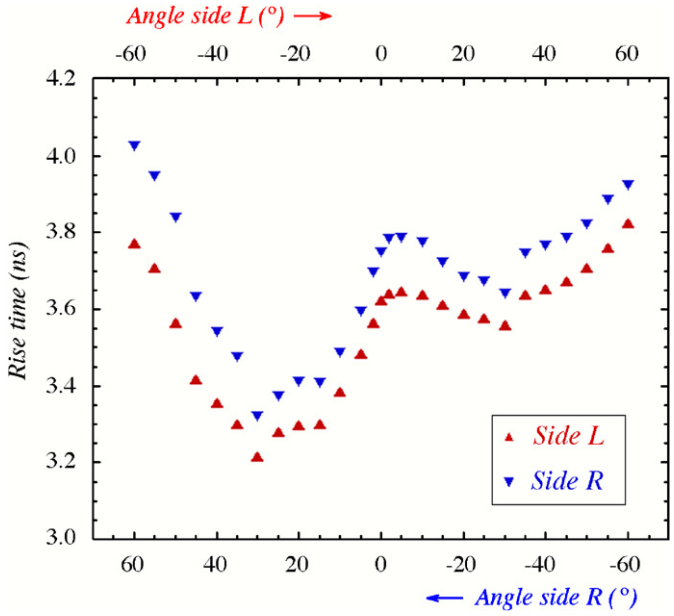

Fig. 8. The average time needed for the PMT signals to rise from 10% to 90% of their amplitude, as a function of the angle of incidence of the beam particles (50 GeV e^-). Results are given for both PMTs, but the angular scales are inverted. The scale on the bottom axis refers to PMT *R*, the scale on the top axis to PMT *L*.

100 mV, equivalent to an energy deposit of ~0.1 GeV was used. The difference between the times at which the signals from PMT *L* and PMT *R* crossed this threshold when the crystal was oriented perpendicular to the beam ($\theta = 0$) was used as reference point for these data. The figure shows the separation power of the time difference Δt_{L-R} for the crystal oriented either at $\theta = 30^\circ$ or -30° and the $\theta = 0$ reference value.

The energy scale was derived on the basis of the fact that, according to Monte Carlo simulations, the 50 GeV electrons deposited on average 0.48 GeV in the crystal when traversing it perpendicularly. This corresponds to a signal amplitude of about 400 mV. If photoelectron statistics were the only factor determining the separation power, one would expect Π to scale with the square root of the deposited energy. The curve drawn in Fig. 10 represents the type of dependence that should be expected in that case. While the curve describes the general tendency of the experimental data points, other factors are playing a role as well. These factors all have the effect of *reducing* the separation power, and therefore the curve makes it possible to determine a lower limit to the Cherenkov photoelectron yield.This lower limit amounts to about 60 photoelectrons per GeV, since $\sqrt{60}$~7–8.

When we use these results to determine the precision with which the Cherenkov contribution to individual signals can be determined, we find ~± 2% for energy deposits of 1 GeV, and better for larger energies. This is based on the observation that (at room temperature) the signals measured at $\theta = \pm 30^\circ$ contained a Cherenkov component of ~15%, whereas the contribution at $\theta = 0^\circ$ was ~3%. This is a considerable improvement with respect to the precision that can be obtained from the other types of measurements discussed earlier in this subsection. However, we should also point out that in a practical calorimeter system based on the dual-readout principles, it will be very hard, if not impossible, to extract the combined information on directionality and time structure that is needed to obtain this type of precision. Moreover, as we will see in the next subsection, the directionality information tends to vanish as the calorimeters become thicker and contain a larger fraction of the developing shower.

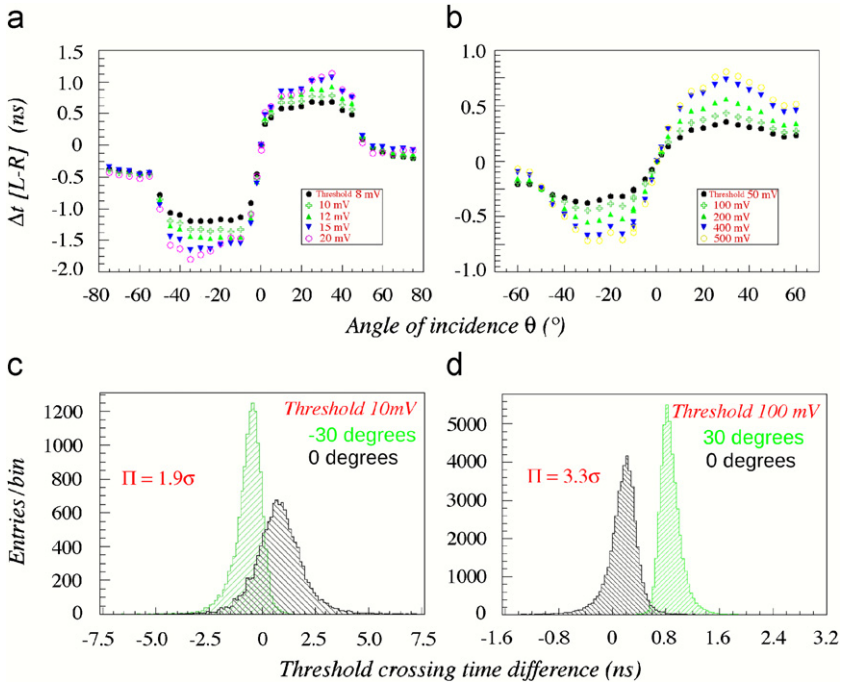

Fig. 9. Time difference between the moments the signals from PMT *L* and *R* cross a preset threshold level. Average results are given as a function of the angle of incidence for mips (a) and 50 GeV e^- (b). Event-by-event distributions are given for mips (c) and 50 GeV e^- (d), for two different angles.

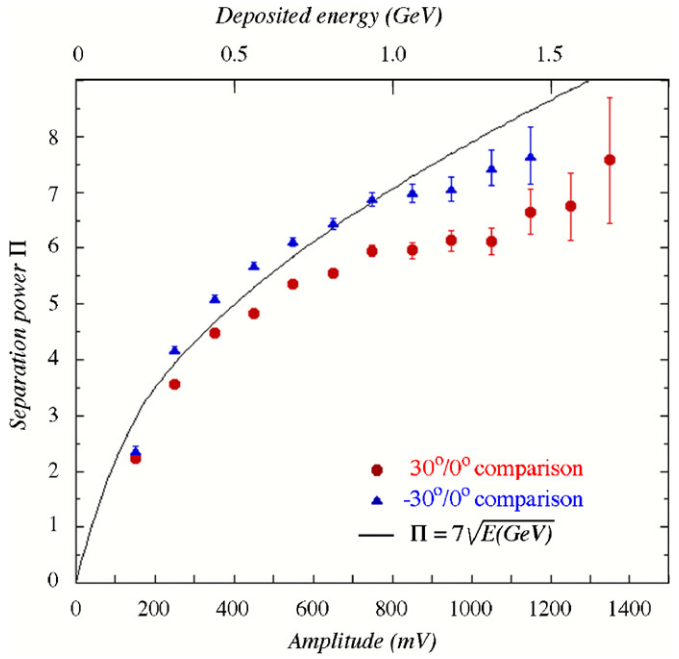

Fig. 10. Separation power between electrons traversing the $PbWO_4$ at angles of $\theta = 0^\circ$ and 30°, as a function of the energy deposited in the crystal, i.e. the amplitude of the signals generated in it. The curve describes the expected energy dependence if photoelectron statistics (in this example for a light yield of 50 Cherenkov photoelectrons per GeV) was the *only* factor determining the separation power.

3.3. Cherenkov signals from developing showers

We have tested the merits of the methods described in the previous subsection (and others based on the time structure of the signals) with data obtained with lead absorbers of various thicknesses installed upstream of the $PbWO_4$ crystal. In this way, different stages of the em shower development were probed by the crystal. For example, with 25 mm of lead ($4.5X_0$) installed in front, the crystal detected light produced at a depth between 4.5 and $7X_0$, i.e. around the shower maximum. In that case, the shower particles producing the light may no longer be considered a collection of mips traversing the crystal all in approximately the same direction, as in the very early part of the shower development. The Cherenkov light was now much more isotropically emitted, since the particles that generated it were more isotropically distributed.

This is illustrated in Fig. 11a, which shows the response *anisotropy*, a measure for the Cherenkov content of the signals defined as

$$\xi(\theta) = \left|\frac{(R_\theta - L_\theta) + (L_{-\theta} - R_{-\theta})}{(R_\theta + L_\theta) + (L_{-\theta} + R_{-\theta})}\right| \quad (1)$$

where R_θ and L_θ represent the average signals measured in the PMTs *R* and *L* for the same events, with the crystal oriented at an angle θ. Since these signals were equalized for $\theta = 0$, a non-zero value of ξ is indicative for a non-isotropic component in the light generated in the crystals, i.e. Cherenkov light. In another paper, we have shown that for mips the anisotropy is directly related to the fraction of Cherenkov light contributing to the signals [4]. Fig. 11a shows the anisotropy at $\theta = 30^\circ$, at which angle it was close to its maximum value, as a function of the thickness of the lead absorber in front of the $PbWO_4$ crystal. As the shower developed, the anisotropy quickly decreased, from ~7–8% in the earliest stage to ~1–2% around the shower maximum and beyond.

3.4. Time structure of the signals from developing showers

We have estimated the Cherenkov content of the crystal signals also on the basis of the time structure, using the methods described in Section 3.1, i.e. by determining the fraction of the total signal collected in the first $\Delta t = 6$ ns for $\theta = 30^\circ$ and comparing it to $\theta = -30^\circ$. The results are summarized in

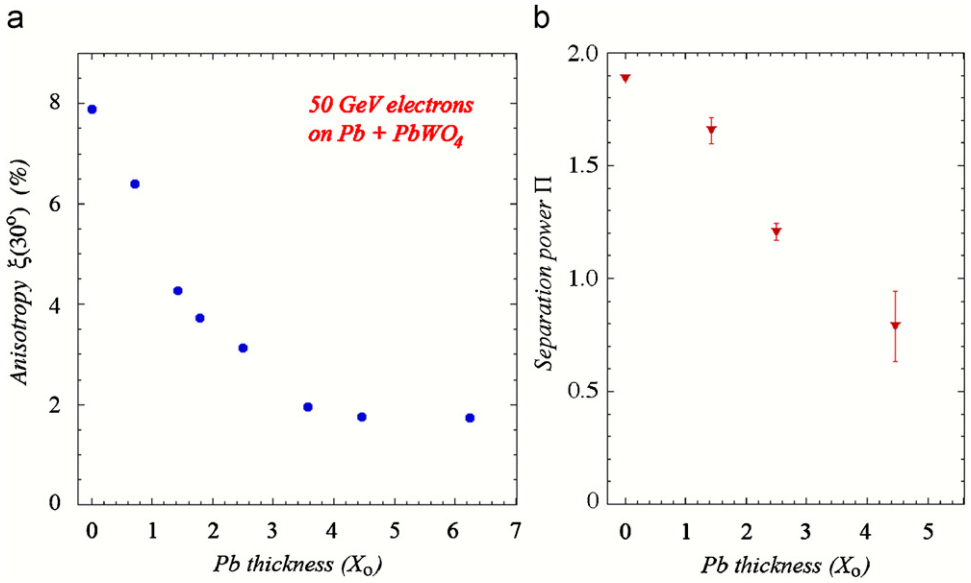

Fig. 11. The response anisotropy ξ at $\theta = 30^{\circ}$, as a function of the thickness of a lead plate placed upstream of the $PbWO_4$ crystal (a), and the separation power based on a comparison of the fraction of the total charge collected in the first 6 ns (b). The error bars indicate the spread observed between the two PMTs. Data for 50 GeV electrons.

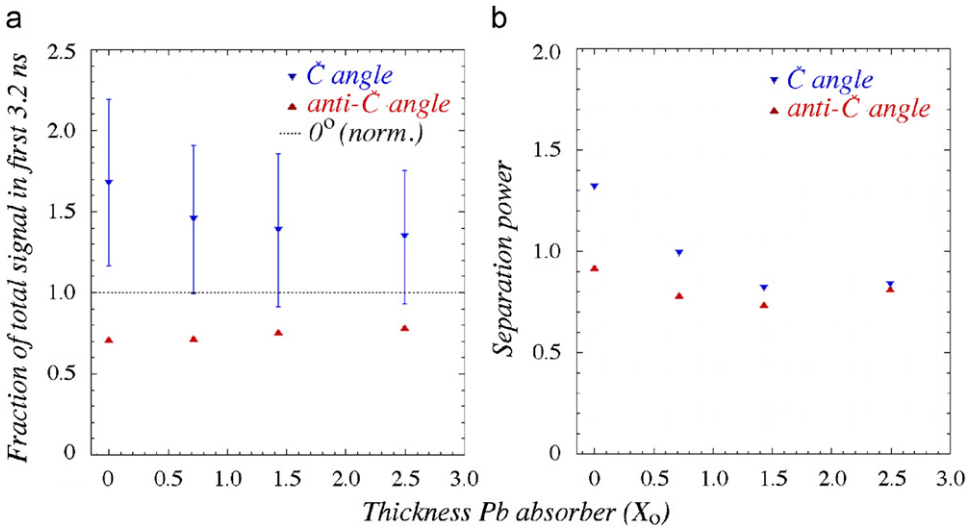

Fig. 12. Measurement of the Cherenkov fraction from the time structure of the $PbWO_4$ signals as a function of the thickness of a lead absorber placed in front of the crystal. The average fraction of the total signal recorded during the first 3.2 ns of the pulse recorded in PMT L, for the Cherenkov angle ($\theta = -30^{\circ}$) and the anti-Cherenkov angle ($\theta = 30^{\circ}$), using the fraction observed at perpendicular incidence ($\theta = 0$) as normalization. The error bars represent the event-by-event spread (σ_{rms}) in the distribution (a). The separation power resulting from these measurements (b). Data for 50 GeV electrons.

Fig. 11b, which shows the separation power that may be derived from this method as a function of the amount of lead installed in front of the $PbWO_4$ crystal. As the lead thickness increased, the separation power decreased. Since the signals increased substantially with respect to those measured without upstream lead, the reduced fluctuations in the numbers of photoelectrons apparently played no significant role for this separation power. The fact that the anisotropy, and thus the difference between signals that supposedly did and did not contain a Cherenkov component, vanished quickly as the amount of lead increased was clearly a much more important factor. Yet, a comparison of Figs. 11a and b suggests that the separation power did not decrease as fast as the anisotropy.

In another approach, we compared the fraction of the signals recorded during the first 8 bins (3.2 ns) with the fraction for a fixed reference signal, for which we chose the signals recorded at perpendicular incidence ($\theta = 0$) and no lead absorber upstream of the crystal. The results of this study are summarized in Fig. 12. Fig. 12a shows the average fraction measured in one of the PMTs (PMT L) at the Cherenkov angle ($\theta = -30^{\circ}$) and at the anti-Cherenkov angle ($\theta = 30^{\circ}$), as a function of the amount of lead placed upstream of the crystal. As expected, this fraction was larger than that for the reference signal at the Cherenkov angle, and smaller at the anti-Cherenkov angle. As the absorber thickness increased, both values moved closer to that for the reference signal, which indicates that the Cherenkov light becomes less directional as one probes a later (deeper) region of the shower development. The error bars in Fig. 12a represent the rms spread in the event-by-event distribution of the measured signal fraction. In Fig. 12b, we have translated these error bars into the separation power achievable by comparing the measured charge fraction with that of our reference signal. This separation

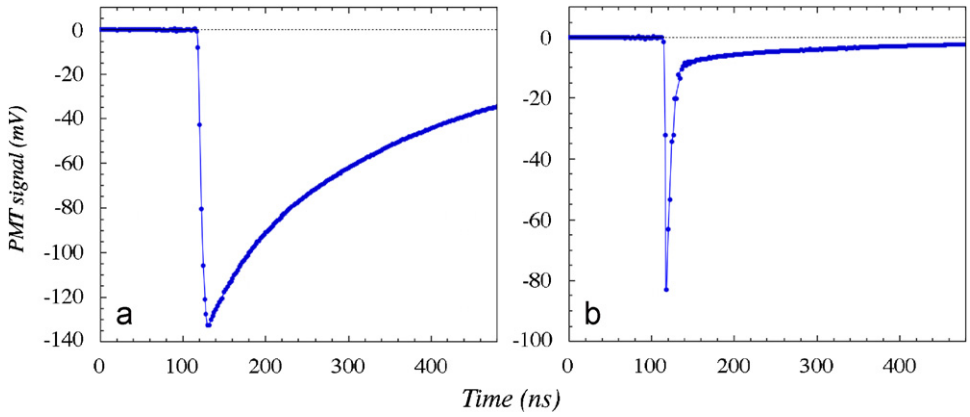

Fig. 13. The time structure of a typical 50 GeV e^- signal measured in the BGO crystal equipped with a yellow filter (a), and with a UV filter (b). These signals were measured with the sampling oscilloscope, with a time resolution of 2.0 ns. The crystal was oriented perpendicular to the beam line ($\theta = 0$).

power, although not very impressive, is fairly independent of the absorber thickness.

In conclusion, we see that methods intended to extract information on the Cherenkov component of the $PbWO_4$ signals that are based on the time structure are less sensitive to the absorber than methods based on the directionality. Whereas the directionality of the Cherenkov component tends to fade as the shower develops, the prompt character of the Cherenkov light is not affected and allows measuring the contribution of this component, albeit not with a very impressive precision.

4. Experimental results for BGO

4.1. The Cherenkov component in the BGO signals

The time structures of the signals from the BGO crystal observed with the yellow filter and the UV filter were very different.

This is illustrated in Fig. 13, which shows the time structures measured from both sides of the crystal (i.e. with the two different filters) for a typical shower developing in it. These features can be understood from the properties of the filters and of the light that is converted into an electric signal.

Fig. 14 shows the transmission characteristics of the two filters as a function of wavelength, as well as the scintillation spectrum of BGO, the spectrum of the Cherenkov light generated in the crystal and the wavelength dependence of the quantum efficiency of the photocathode used in the PMTs. The scintillation spectrum of BGO is centered around a wavelength of 480 nm, i.e. in the yellow/green domain. The decay time of the scintillation process is ~300 ns. The yellow filter is highly transparent for this type of light, as reflected by the signal shape in Fig. 13a.

The UV filter is transparent for light in the wavelength region around 300 nm, and also has a window around 700 nm, where the transmission coefficient is a few percent of that in the ultraviolet region, and the quantum efficiency of the photocathode is also at the level of 1% of that around 350 nm. As a result, this filter is highly transparent for Cherenkov light in the 300–400 nm range, and for wavelengths 320–400 nm the probability that photons reaching the photocathode produce a photoelectron exceeds 10%. On the other hand, only a very small fraction (<0.1%) of the scintillation light penetrates this filter.

Even though Cherenkov light represented a very small fraction of the total light production in this BGO crystal, it was therefore prominently present in the signals from the PMT that read out the side where the UV filter was mounted. This is illustrated by

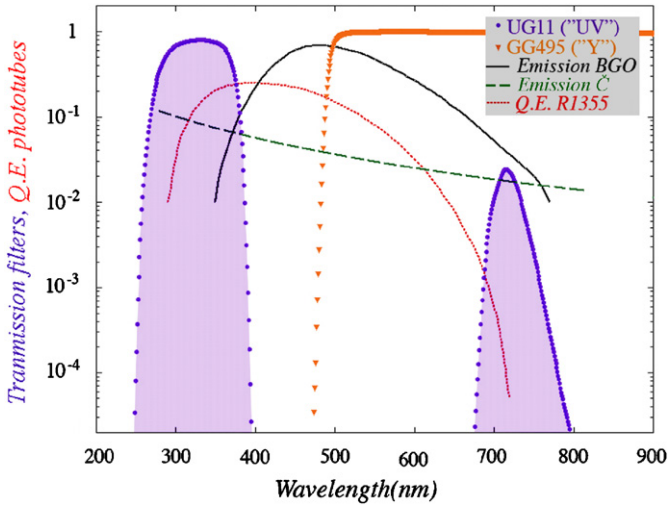

Fig. 14. Light transmission as a function of wavelength for the two filters used to read out the BGO crystal. The light emission spectrum of the crystal, the spectrum of the Cherenkov light generated in it and the quantum efficiency of the PMTs used to detect this light are shown as well. The vertical scale is absolute for the transmission coefficients and the quantum efficiency, and constitutes arbitrary units for the light spectra.

the time structure of the signals in Fig. 13b, where the sharp peak represents the prompt Cherenkov signal component.

In order to see if this prompt peak was indeed caused by Cherenkov light, we studied its angular dependence. The crystal was rotated around the y-axis, from $\theta = -45^\circ$ to $+60^\circ$, in steps of 5° (see Fig. 1). In order to limit the contribution of scintillation light to the UV signals, the ADC gate was adjusted so that the signals were integrated up to $t = 120$ ns (i.e. over the first ~10 ns after the start of the pulse, see Fig. 13), Fig. 15 shows the ratio of the ADC signals from the UV and Y sides of the crystal as a function of θ. It clearly illustrates the directional nature of the light contained in the "prompt" UV signal component. It peaks near $\theta \approx 28^\circ = 90^\circ - \theta_C$, as one would expect for Cherenkov light.

More detailed, quantitative information was derived from the time structure of the signals. The oscilloscope measurements made it possible to determine the contribution of scintillation light to the UV signal in a narrow gate around the prompt peak *event-by-event*. This could be done by normalizing the shape of the time structure of pure scintillation light, which was well known from the signals measured with the yellow filter, to the tail

of the time structure of the UV signals. This is illustrated in Fig. 16a for mip signals measured at $\theta = 0^\circ$. The "contamination" of scintillation light in the UV signals measured this way is given as a function of the width of the chosen window around the prompt peak in Fig. 16b. This figure also shows the fraction of the Cherenkov light collected during this time. For example, for a gate width of 20 ns, enough to collect >99% of the Cherenkov light produced in these events, ~20% of the UV signal consisted of scintillation light.

This method made it possible to measure the Cherenkov/scintillation ratio of the UV signals for individual events, using only the time structure of these signals. Fig. 17 shows the average ratio as a function of the angle θ, for 50 GeV electrons and 200 GeV pions, using a gate width of 10 ns around the prompt peak. The distribution for the electron signals looks very similar to the one from Fig. 15, albeit that the signal ratios are much larger in this case. A detailed comparison between the distributions for electrons and pions shows some interesting differences:

- The angular distribution of the $\check{C}/S$ signal ratio is somewhat broader for electrons than for mips. This is most likely due to the fact that shower particles traveling at an angle with respect to the beam contributed significantly to the electron signal.
- The $\check{C}/S$ signal ratio for electrons has a larger value than that for pions in the angular region where one would naively expect to detect no Cherenkov light at all, i.e. for $\theta < 0$. This probably has the same origin as the previous phenomenon, since the Cherenkov light was more directional in the case of the pions. This led to a more pronounced angular dependence of the collection efficiency.
- The angular distribution for electrons shows variations outside statistics in the range from 20° to 35°, which seems to be somewhat less pronounced, but not absent, for the mip case. The point-to-point fluctuations are significantly larger than the statistical uncertainties, so that this angular structure must be the result of some systematic effect. Our measurements have shown the structure to be very reproducible. We suspect that details of the light collection mechanism are responsible for this substructure (see Section 5).

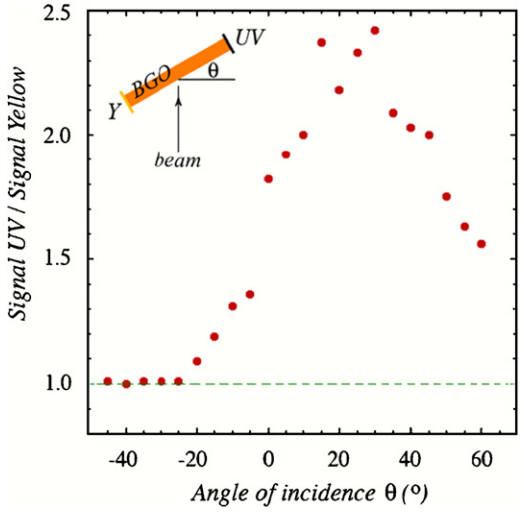

Fig. 15. Ratio of the ADC signals observed at the two exit surfaces of the BGO crystal, which were equipped with a UV filter and a yellow filter, respectively, as a function of the angle of incidence of the 50 GeV electrons. This ratio was normalized to a value of 1.0 for $\theta = -40^\circ$.

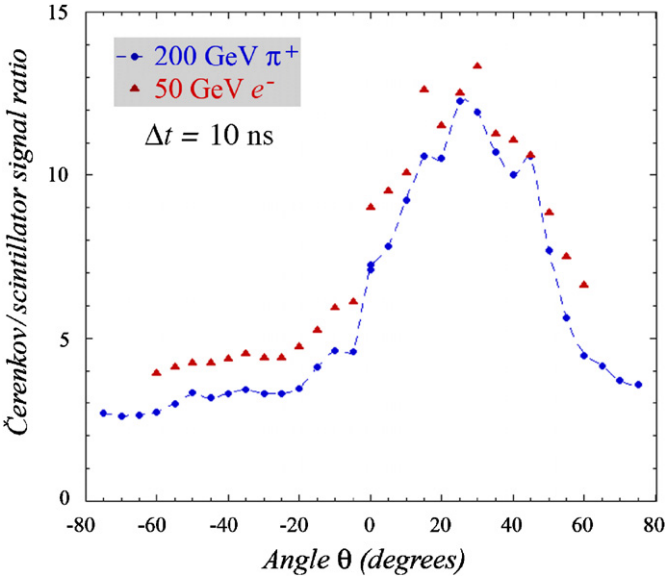

Fig. 17. The Cherenkov/scintillation ratio in the UV signals from the BGO crystal, for a gate of 10 ns around the prompt peak, as a function of the orientation of the crystal with respect to the beam. Data for 50 GeV electrons and 200 GeV π^+.

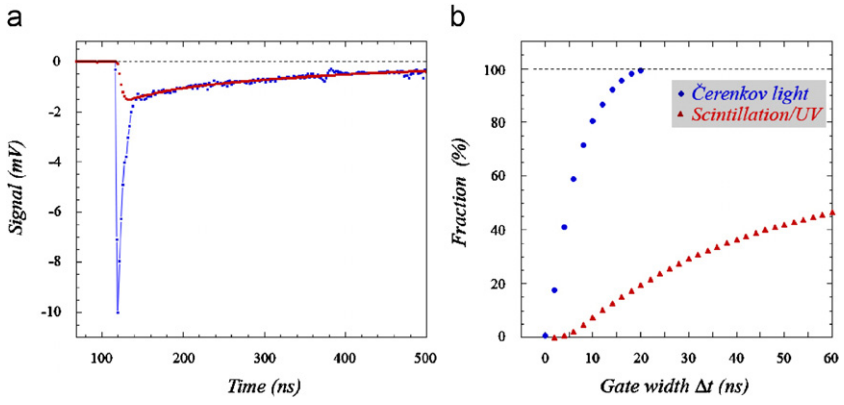

Fig. 16. The average time structure of the UV signals from 200 GeV π^+ at $\theta = 0^\circ$, together with the time structure of the scintillation component contributing to this signal (a). Such data made it possible to determine the "contamination" of scintillation light in a narrow window with width Δt around the prompt peak (b). Shown are the (average) fraction of the total UV signal that was caused by scintillation light, as well as the (average) fraction of the Cherenkov light collected as a function of this gate width.

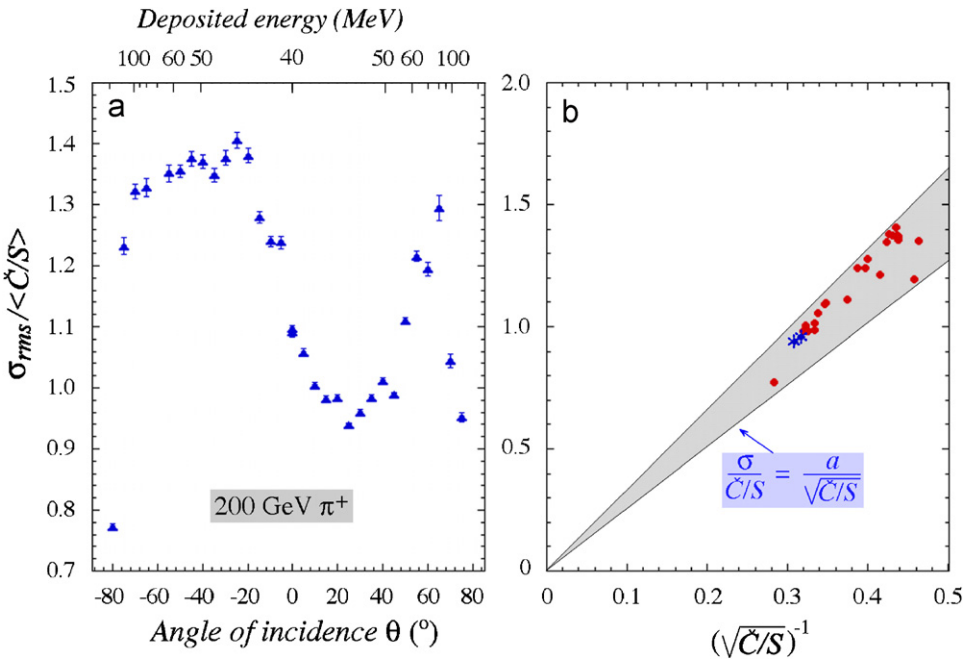

Fig. 18. The relative width of the distribution of the $\check{C}/S$ ratio for 200 GeV π^+ traversing the BGO crystal, as a function of the angle θ (a) and as a function of $(\check{C}/S)^{-1/2}$ (b). The average energy loss of the particles for different orientations of the crystal is indicated on the top axis. Data for a gate width of 20 ns around the prompt Cherenkov peak. The asterisks denote the data points for $\theta = 25^\circ$ and 30°.

4.2. The Cherenkov light yield

We have tried to assess the (Cherenkov) light yield of this crystal quantitatively. After all, we are pursuing the option to use crystals for dual-readout purposes because the Cherenkov light yield (8 photoelectrons/GeV) was a limiting factor for the resolution of the fiber calorimeter with which the virtues of dual-readout calorimetry were first demonstrated [2]. In order to determine the light yield, we have measured the event-to-event fluctuations in the $\check{C}/S$ signal ratio as a function of the size of the UV signal. This was done both for the small signals generated by mips (40–100 MeV, depending on the path length) and for the somewhat larger signals from electrons, which deposited typically ~900 MeV on their way through the crystal (at $\theta = 30^\circ$). We have explored several different methods to assess the contribution of fluctuations in the number of Cherenkov photoelectrons, as described below.

Fig. 18a shows the relative width ($\sigma_{\rm rms}$/mean) of the distribution of the $\check{C}/S$ ratio for 200 GeV pions traversing the BGO crystal, as a function of the angle θ (i.e. the path length). These data were obtained for a gate width $\Delta t = 20$ ns around the prompt Cherenkov peak. At this gate width, >99% of the Cherenkov light was collected. At $\theta = 0^\circ$, $\langle\check{C}/S\rangle \approx 6$ (see also Fig. 17), while this ratio reached a maximum value of ~10 for $\theta = 25$–30°. The figure shows that the relative width $\sigma/\langle\check{C}/S\rangle$ also dips around the angular region where the Cherenkov component in the signals was the largest.

The average energy loss of the pions is proportional to the path length in the crystal, i.e. proportional to $(\cos\theta)^{-1}$. This energy loss is indicated on the top axis of Fig. 18a. Minimum ionizing particles lose, on average, 9.0 MeV/cm in BGO. Therefore, when mips traverse the crystal perpendicularly in the center, they lose, on average 25 MeV. However, 200 GeV pions are *not* mips, they lose more energy. We have estimated the average energy loss by these particles to be 40 MeV, on the basis of the energy calibration discussed below.

If fluctuations in the numbers of photoelectrons were the *only* contribution to the width of the $\check{C}/S$ distribution, we should expect $\sigma/\langle\check{C}/S\rangle$ to scale with $(\check{C}/S)^{-1/2}$. This can be checked from Fig. 18b, where $\sigma/\langle\check{C}/S\rangle$ is plotted as a function of $(\check{C}/S)^{-1/2}$. The experimental data seem to be reasonably described by this relationship, although it should be pointed out that the proportionality constant a is a function of the angle θ. This proportionality constant makes it possible to estimate the Cherenkov light yield. Since the horizontal axis describes the inverse square root of the number of Cherenkov photoelectrons,

$$a = \left[\frac{0.041 S^*}{\cos\theta}\right]^{-1/2} \tag{2}$$

where S^* represents the average number of *scintillation* photoelectrons detected in the 20 ns time window, per GeV of energy deposited in the crystal. As we saw before, the average energy deposited amounts to $0.041/\cos\theta$ GeV, and the number of *Cherenkov* photoelectrons associated with that is thus $(\check{C}/S) \times S^* \times 0.041/\cos\theta$.

From Fig. 18b, we found $a(30^\circ)$ to be 3.0, which leads to $S^* = 2.3$ p.e. per GeV. Since $\langle\check{C}/S\rangle$~12 at this angle (Fig. 17), we conclude that the Cherenkov light yield is ~28 photoelectrons per GeV. It is important to realize that this is a lower limit, since any contribution from sources other than photoelectron statistics to the measured values of $\sigma/\langle\check{C}/S\rangle$ would *increase* this calculated light yield. One obvious contribution comes from the fact that the energy deposit spectrum in the crystal is *not* Gaussian, but has a Landau tail. If we had derived the values of $\sigma/\langle\check{C}/S\rangle$ from a Gaussian fit around the most probable energy loss, they would have been considerably smaller, and the light yield derived from an analysis as described here would have been correspondingly larger.

A second method to estimate the light yield was applied to the signals produced by 50 GeV electrons. The signal distribution from electrons traversing the BGO crystal looked very similar to the one shown in Fig. 3a. We subdivided the horizontal scale into 60 bins of equal width and measured the distribution of the Cherenkov/scintillation signal ratio for each of these bins. The fractional

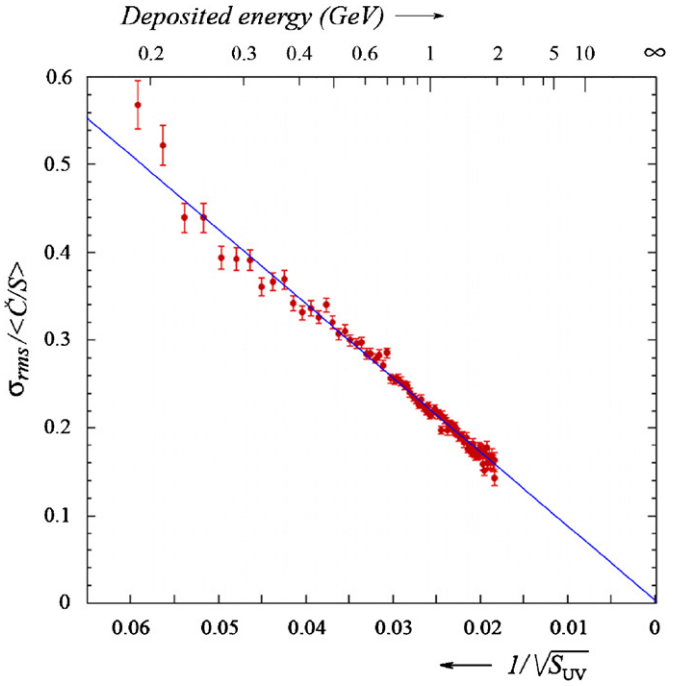

Fig. 19. The fractional width of the distribution of the $\check{C}/S$ ratio for 50 GeV electrons traversing the BGO crystal, as a function of the total UV signal. The corresponding energy loss is indicated on the top axis. The crystal was oriented at $\theta = 30^{\circ}$, and the $\check{C}/S$ ratios were determined for a gate width $\Delta t = 20$ ns around the prompt peak.

width ($\sigma_{\rm rms}$/mean) of this distribution is shown as a function of the total UV signal in Fig. 19.

This signal (which is proportional to the deposited energy) is plotted on a scale linear in its inverse square root, so that scaling with $E^{-1/2}$ implies the data points to be located on a straight line through the bottom right-hand corner. The experimental data are indeed well described by such a straight line, any energy-independent deviations ("constant term") are statistically insignificant. The relationship between the signal units and the deposited energy was established with a GEANT-4 Monte Carlo simulation of the development of em showers in a 2.7 cm thick BGO crystal, which showed that, on average, 0.886 GeV was deposited in this process.[13]

The energy dependence of the fractional width of the $\check{C}/S$ ratio in the UV signals was found to scale with the inverse square root of the total UV signal (and thus of the energy deposited by the electrons):

$$\frac{\sigma_{\rm rms}}{\langle C/S\rangle} = \frac{0.220}{\sqrt{E}} \tag{3}$$

with the energy E given in GeV. This relationship is represented by the fitted curve in Fig. 19. Since the ratio of the numbers of Cherenkov and scintillation photoelectrons in the total UV signals at this angle was about 0.44, and assuming that the energy dependence is entirely due to fluctuations in the *total* number of photoelectrons in the UV signal, we conclude that at 1 GeV

$$\frac{1}{\gamma_{\rm S}} + \frac{1}{0.44\gamma_{\rm S}} = (0.220)^2 \tag{4}$$

so that the average number of scintillation photoelectrons ($\gamma_{\rm S}$) for a 1 GeV em energy deposit was 68 and the average number of Cherenkov photoelectrons 30. This is a substantial improvement with respect to the light yield of the fiber-based DREAM calorimeter, which would reduce the contribution of (Cherenkov) photoelectron statistics to the energy resolution of a dual-readout calorimeter from $35\%/\sqrt{E}$ to $\sim 18\%/\sqrt{E}$.

4.3. The precision of $\check{C}/S$ measurements

The (Cherenkov) light yield is also very important for the precision with which the Cherenkov content of the signals can be measured in individual events. The analyses performed in the previous subsections provided the relevant results for the assessment of this precision. For example, from Fig. 19, we conclude that the Cherenkov/scintillator ratio for an energy deposit of 1 GeV can be measured with a relative precision of ~22%, in events where this energy is deposited by (a collection of) mips traveling in such a direction that the detection efficiency of Cherenkov light is optimized, i.e. for $\theta = 30^{\circ}$. Fig. 17 shows that the specific Cherenkov light yield was about a factor of three smaller at angles $< -20^{\circ}$, which reduces the precision at 1 GeV according to Eq. (4) to ~34%.

In order to check this assessment, we repeated the calculation of the relative fluctuations in the $\check{C}/S$ ratio for a number of other angles. Fig. 20a shows the value of $\sigma_{\rm rms}$/mean for an energy deposit of 1 GeV as a function of the angle of incidence of the 50 GeV electrons. An example of one event-by-event distribution from which this parameter was determined (for $\theta = 30^{\circ}$) is given in Fig. 20b. According to Fig. 20a, the relative precision with which the $\check{C}/S$ value could be measured reaches a minimum value of ~22% around the Cherenkov angle, and increases at negative angles to ~30%. The latter value is somewhat smaller than expected on the basis of Eq. (4). This might indicate that factors other than photoelectron statistics contributed to the widths of the $\check{C}/S$ distributions. This, in turn, would imply a larger light yield than we estimated on the basis of Eq. (4). The quoted value of 30 Cherenkov photoelectrons per GeV should thus be considered a lower limit. In that context, it is also important to mention that, since the PMT only covered ~65% of the UV exit surface of the BGO crystal, the Cherenkov light yield would anyway increase correspondingly with a larger PMT.

5. Instrumental effects

The precise value of the Cherenkov contribution to the signals from a given crystal depends on a large number of factors, of which we mention: details of the manufacturing process, the temperature, the type of light detector used to collect the signals, a variety of properties of this light detector (size, wavelength and position dependence of the quantum efficiency), the type and angle of incidence of the particles that generate the signals, the crystal's transparency for the different types of light, etc.

The main purpose of the present study was *not* to measure the actual (average) value of the Cherenkov/scintillation signal ratio, but rather the precision with which this ratio can be measured for individual events in a given setup, with specific light detectors and for specific particles generating the signals. This precision is important for the possible application of these crystals as dual-readout calorimeters. Another parameter that is important for this type of application is the Cherenkov light yield. That is why we have concentrated on these aspects in this analysis.

Should one decide to develop the crystals discussed in this paper into dual-readout calorimeters, then some instrumental effects that play an important role in these crystals would have to be taken into consideration. In this section, we discuss two of these effects: light attenuation and reflections.

[13] This result also formed the basis of the determination of the energy loss by 200 GeV π^+.

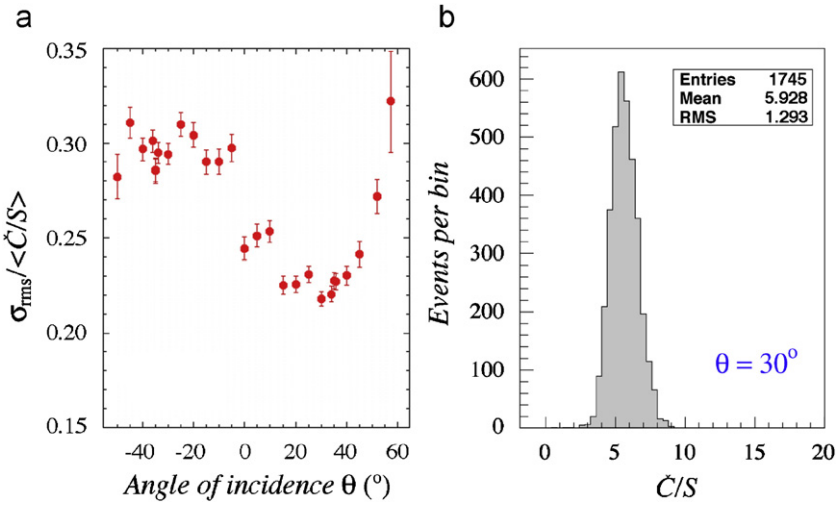

Fig. 20. The fractional width of the distribution of the $\check{C}/S$ ratio for 50 GeV electrons traversing the BGO crystal and depositing 1 GeV, as a function of the angle of incidence (a), and the distribution of this ratio for these events at $\theta = 30^{\circ}$ (b).

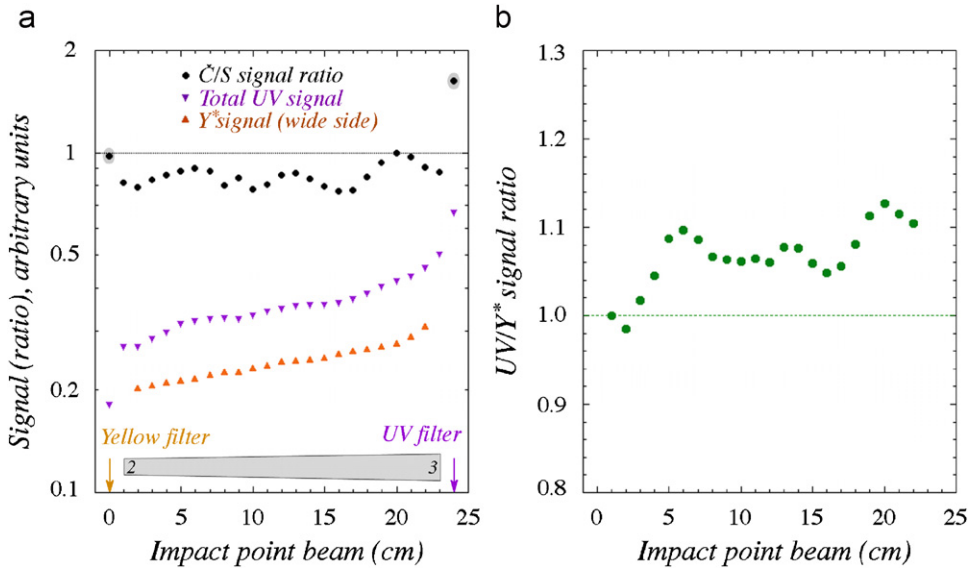

Fig. 21. The total UV signal, and the ratio of the signals from Cherenkov and scintillation light measured with the PMT on the UV-filter side of the BGO crystal, as a function of the distance traveled by the light from the production point to the PMT. The positions of the filters for these measurements, as well as the crystal orientation, are indicated. Also shown is the total yellow signal (Y^*) for the same crystal orientation and impact points, but with the filter positions exchanged (a). The ratio of the UV and Y^* signals shown in diagram a, i.e. the ratio of the two signals after geometrical effects have been eliminated (b). Data for 50 GeV electrons at $\theta = 0$.

5.1. Light attenuation

The short-wavelength Cherenkov light that formed the source of the signals we have analyzed was possibly considerably attenuated on its way from the production center to the light detector. This might give rise to systematic effects in applications (e.g. dual-readout calorimetry) of this signal. We have studied the BGO signals, and in particular also the ratio between the Cherenkov and scintillation components of the UV signals, as a function of the impact point of the beam particles, i.e. as a function of the distance the light had to travel to the UV filter and its associated PMT. The crystal was oriented perpendicular to the beam ($\theta = 0$) and was moved in steps of 1 cm in the x-direction (see Fig. 1). The ratio of the two signal components was determined from the time structure of the UV signals, as described before (Fig. 16).

In order to eliminate possible effects resulting from the tapered shape of the crystal, these measurements were also performed with the two filters in reversed positions, i.e. the yellow filter mounted on the wide ($3.2 \times 3.2\,cm^2$) exit surface of the crystal and the UV filter on the narrow $2.4 \times 2.4\,cm^2$ one. In all other measurements described here, the UV filter was mounted on the $3.2 \times 3.2\,cm^2$ surface. The results of these studies are summarized in Fig. 21.

Fig. 21a shows that the total UV signal changed by almost a factor of two over the 24 cm long crystal. However, most of this effect was geometrical, i.e. the result of the fact that the crystal was ~30% thicker on one end compared to the other. A measurement of the yellow scintillation light with the filters in reversed position (called the Y^* signal in the figure) made it possible to eliminate the geometrical component of this effect. The result, shown in Fig. 21b, indicates that indeed most of the factor two change in the UV signal was of geometrical origin and that genuine attenuation effects decreased the UV signal by ~10% over the 24 cm length of the crystal. The unusual position

dependence is possibly the result of differential polishing procedures applied by the L3 Collaboration from which this crystal was obtained. It illustrates that attenuation effects with such techniques might eventually be reduced to insignificant proportions.

Fig. 21a also shows the ratio of the Cherenkov and scintillation components of the UV signal as a function of the distance between the production center of the light and the PMT that converted this light into electric signals. It turned out that this ratio was fairly constant over the full length of the crystal. We conclude from this that possible contributions from the far-red window of the UV filter (see Fig. 14), which would cause differences between the attenuation characteristics of both components, were negligible. The observed oscillatory pattern that seems to be superimposed on the constant $\check{C}/S$ signal ratio clearly derived from the characteristics of the Cherenkov component. It may be explained from the fact that the photocathode of the PMT only covered ~65% of the wide exit surface of the BGO crystal. Because of the directionality of the Cherenkov light, the "beam spot" it projected onto this exit surface moved with the position where the light was produced (and thus the distance it had to travel to reach this exit surface). Since the Cherenkov light was emitted at an angle of 62°, one should in a crystal with thickness d expect a pattern with a period of $2d\cot 28^\circ/\sqrt{2}$~7.5 cm, in good agreement with the experimental observations.[14]

This explanation for the position dependence of the $\check{C}/S$ signal ratio would also affect its angular dependence, since the position of the "beam spot" is obviously quite sensitive to the *direction* of the particles emitting the Cherenkov light. This may well explain the "fine-structure" observed in Figs. 15 and 17.

Interestingly, the $\check{C}/S$ signal ratio increased substantially for the measurements closest to the two end faces of the crystal, especially at the end face connected to the PMT from which the signals are displayed here. This is due to the fact that the filters and the glass windows of the PMTs also served as a production source of Cherenkov (but no scintillation) light. The fact that the increase of the signal ratio was less important at the far end of the crystal is due to the absorption of most of this additional Cherenkov light by the yellow filter.

5.2. Reflections

Until now, we have ignored the effects of light reflection at the interface between the crystal and the readout elements. However, because of the large index of refraction ($n = 2.2$ in $PbWO_4$, 2.15 in BGO), such effects are not at all negligible. Light traveling along the crystal axis experienced a (Fresnel) reflection coefficient of 13% (4% when cookies were installed between the crystal and the PMT), and the reflection coefficient increased with the angle of incidence, to reach 100% at the critical angle. Internal reflections may explain several aspects of the data presented in this paper. For example, the fact that Cherenkov light was observed in the time structure of the BGO signals from mips at negative angles (Fig. 17) is probably the result of reflection of this light off the interface where the yellow filter was located (the L position in Fig. 1).

An example of the consequences of internal reflections in the $PbWO_4$ crystal is given in Fig. 22, which shows the fraction of the PMT signal contained in the prompt component as a function of the angle of incidence of the particles. This prompt (Cherenkov) component was determined by comparing the time structure of the signal with that of a reference, supposedly "pure" scintillation,

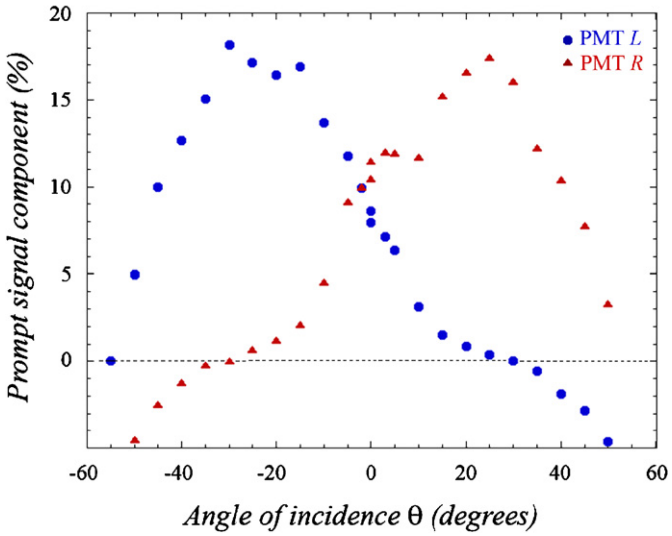

Fig. 22. The Cherenkov/scintillator signal ratio as a function of the angle of incidence of the beam particles (50 GeV e^-), derived from the average time structure of the signals. Results are given separately for the two PMTs reading out the $PbWO_4$ crystal. The time structure of the signals at $\theta = 30^\circ$ (-30°) served as the scintillation reference for PMT L (R).

signal. For PMT L, the signal at $\theta = 30^\circ$ was used as such a reference, for PMT R, the signal at $\theta = -30^\circ$ (see also Fig. 4). However, Fig. 22 shows that the prompt component reached actually a secondary maximum at these "anti-Cherenkov" angles, i.e. the angle at which the prompt component in the signal from the PMT at the opposite end of the crystal reached it maximum value. Reflection of the Cherenkov light at the crystal/PMT interface would cause precisely such a phenomenon. The same effect was also observed in our measurements on the BGO crystal.

More evidence for the role of reflections in the measurements on the $PbWO_4$ crystal can be derived from Figs. 5 and 8. In both cases, the same phenomena characteristic for the Cherenkov angle were also observed, albeit much weaker, at the anti-Cherenkov angle. It is interesting to note that these effects disappeared for very short gate times (Fig. 5b), presumably since the light had to make an extra roundtrip through the crystal to cause this effect. This led to a delay of several ns.

The importance of internal reflections in the crystal became very evident when we investigated the role of the silicone cookies, as illustrated in Fig. 23. Fig. 23a shows the average time structure of the prompt UV signal component of the BGO signals from 50 GeV electrons traversing the crystal perpendicularly ($\theta = 0$), measured with and without these cookies installed between the crystal and the filter and between the filter and the PMT. The measurement without the cookies revealed an oscillating pattern which was absent for the measurement with the cookies in place.

In Fig. 23b, the time structure of the cookie-less measurement is shown after eliminating the contribution of scintillation light to the signals. The time structure of the remaining Cherenkov component is shown on a logarithmic scale in this figure. The trailing edge of this structure is well described by a number of equally spaced peaks, superimposed on an exponentially decreasing curve. The peaks are separated by 4.0 ns, which corresponds to the time light travels a distance of $4.0 \times 30/2.15 = 55.8$ cm in BGO. Since the crystal was 24.0 cm long, this means that the light responsible for these reflections traveled on average at an angle of $\arccos 48/55.8 = 30^\circ$ with the crystal axis. This is very close to the critical angle for total reflection in the cookie-less crystal (28°). A large fraction of the Cherenkov light emitted by the showering electrons did indeed impinge on the exit surface at an angle close

[14] In two dimensions, the expected period is $2d\cot 28^\circ$, the factor $\sqrt{2}$ derives from the extension to three dimensions.

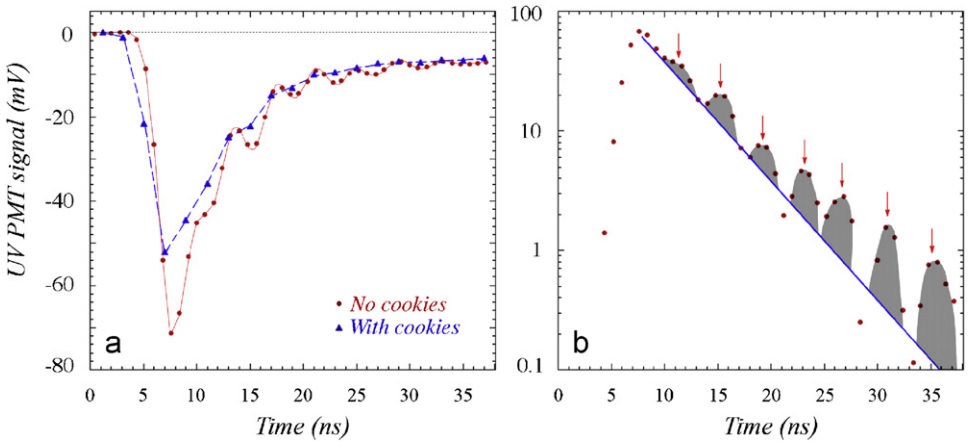

Fig. 23. Average time structure of the prompt component of the UV signals from 50 GeV electrons recorded with and without silicone "cookies" mounted between the BGO crystal, the UV filter and the PMT (a). Logarithmic display of the (inverted) Cherenkov signal measured without the cookies (b). See text for details.

to 28°, the complement of the Cherenkov angle at which this light was emitted.

We conclude from this that the reflections observed in Fig. 23 are predominantly caused by light traveling close to the critical angle, where the reflection probability was very substantial, and the probability for several reflections preceding detection significant. Small changes in the angle of incidence with respect to the exit surface, which may result from the semi-conical shape of the crystal might also have played a role in this.

The time structure shown in Fig. 23b also made it clear that the "non-prompt" nature of the Cherenkov peak is the result of light attenuation in the BGO crystal. The time constant of the exponential curve onto which the various reflection peaks are superimposed equals 4.3 ns. During this time, the light traveled a distance of ~60 cm in the BGO crystal. An exponential fit to the "crests" of the reflection peaks gave a time constant of 6.1 ns (85 cm), while the time structure of the pulse measured in the configuration with the cookies was best described with an exponential with a time constant of 5.5 ns (76 cm). We conclude from these data that the attenuation length of the filtered Cherenkov light in this crystal was around 80 cm. Independent measurements of the light transmission as a function of wavelength in this crystal, carried out with a spectrophotometer, showed that the attenuation length varied from 36 (at $\lambda = 350$ nm) to 76 cm ($\lambda = 400$ nm) in the wavelength region of interest for the filtered Cherenkov light, and leveled off at 100–120 cm for longer wavelengths.

The cookie-less measurement was repeated at different impact points, in which the beam was moved in steps of 1 cm over the total (24 cm) length of the crystal (see Section 2.3). The pattern shown in Fig. 23 remained unchanged in this process, but the position of all peaks shifted as the distance from the impact point to the UV filter was changed, in a manner consistent with the time differences expected for light traveling at a speed c/n. Our analysis of these data showed that light traveled at a speed of 13.3 cm/ns in this crystal, whereas one would expect 13.9 cm/ns on the basis of an index of refraction of 2.15. Since the time base of the scope was started by the trigger counters, these phenomena clearly confirmed that the peaks are the result of (multiple) reflections in the crystal.

6. Conclusions

Dense, high-Z crystals such as $PbWO_4$ and BGO produce significant amounts of Cherenkov light, in addition to the scintillation light that makes them well suited as particle detectors. We have investigated several methods to extract the Cherenkov information from the signals produced by these crystals. BGO turned out to be more favorable in this respect, because

(1) the spectra of the two types of light are quite different, which made it possible to produce clean signals of about equal strength with the help of an optical filter; and,
(2) the decay time of the scintillation process is conveniently long, so that the two components could be easily distinguished and separated on the basis of the time structure of the (filtered) signals.

We have shown that the ratio of the Cherenkov and scintillation signals, a quantity of crucial importance for the application of such crystals as dual-readout calorimeters, can be measured with good precision down to very small energy deposits. We measured this ratio in individual events with a relative accuracy of ~20–30% for energy deposits of 1 GeV in BGO.

The lead tungstate crystals we tested had somewhat less favorable properties than BGO. Although the Cherenkov fraction of the total signal was considerably larger for this crystal, the absence of the two advantages listed for BGO made it harder to extract precise information on the Cherenkov content of individual event signals, although good results were obtained with a combination of information on the directionality and the time structure of the signals.

Both types of crystals generated Cherenkov signals of at least 30 photoelectrons per GeV deposited energy. This is sufficient for reducing photoelectron statistics to a non-dominant source of fluctuations in hadronic dual-readout calorimeters, which was one of the main goals for embarking on this study.

There are ideas on how to improve the properties of $PbWO_4$ crystals with respect to dual-readout calorimeter applications. For example, dedicated dopants in the right concentration could both alter the emission spectrum and the decay time of the pure $PbWO_4$ crystals [5]. However, the practical value of this remains to be demonstrated. It is also clear that instrumental effects of the type discussed in Section 5 are potentially a limiting factor for the success of crystal-based dual-readout calorimeters [6].

Acknowledgments

We thank CERN for making particle beams of excellent quality available for the study described in this paper. This study was

carried out with financial support of the United States Department of Energy, under Contract DE-FG02-07ER41495.

References

[1] N. Akchurin, et al., Nucl. Instr. and Meth. A 582 (2007) 474.
[2] N. Akchurin, et al., Nucl. Instr. and Meth. A 537 (2005) 537.
[3] N. Akchurin, et al., Nucl. Instr. and Meth. A 584 (2008) 273.
[4] N. Akchurin, et al., Nucl. Instr. and Meth. A 593 (2008) 530.
[5] M. Nikl, et al., J. Crystal Growth 229 (2001) 312.
[6] R. Wigmans, New J. Phys. 10 (2008) 025003.